Int J Adv Manuf Technol (2012) 62:887–899
DOI 10.1007/s00170-011-3864-7

ORIGINAL ARTICLE

Prediction and experimental validation of micro-milling cutting forces of AISI H13 steel at hardness between 35 and 60 HRC

S. M. Afazov · S. M. Ratchev · J. Segal

Received: 21 September 2011 / Accepted: 12 December 2011 / Published online: 28 December 2011

Abstract This paper presents prediction and validation of micro-milling cutting forces of AISI H13 steel at hardnesses between 35 and 60 HRC. The cutting forces are predicted based on an approach considering the full kinematics of the cutting tool including the run-out effect, effects of the cutting velocity and tool geometry, ploughing and chip formation phenomena and the hardness of the AISI H13 steel. A plane strain dynamic thermo-mechanical finite element (FE) model of orthogonal cutting is used to predict the cutting forces where the geometry of the cutting tool edge is modelled based on scanning electron microscope measurements. A constitutive elastic–plastic isotropic material model describing the relationship between stresses, strains, strain rates and hardnesses is modelled and implemented into ABAQUS/Explicit FE code by the user-defined subroutine VUMAT. Finite element analyses (FEA) are employed to obtain the relationship between cutting forces, uncut chip thickness, cutting velocity and material hardness. Numerous FEA are performed at different uncut chip thicknesses (0–20 μm), cutting velocities (104.7–4,723 mm/s) and hardnesses (35–60 HRC) using the FE model of orthogonal cutting. The full kinematics of the cutting tool including the run-out effect and the FE-predicted cutting forces are incorporated to predict the micro-milling cutting forces. The predicted micro-milling cutting forces have been experimentally validated at hardness of 43.2 HRC at different feed rates and spindle speeds. The result showed that the cutting forces and cutting temperatures increase by increasing the hardness of the AISI H13 while the stability limits of the process decrease by increasing the hardness.

S. M. Afazov (✉) · S. M. Ratchev · J. Segal
Manufacturing Research Division, Faculty of Engineering,
University of Nottingham,
Nottingham NG7 2RD, UK
e-mail: shukri.afazov@nottingham.ac.uk

Keywords Micro-milling · Cutting forces · Hardness · AISI H13 steel · Finite element analyses

1 Introduction

The micro-milling process is widely used for manufacturing miniature components with complex 3D shapes. The demand for fabricating products and features at the micro-scale level has pushed manufacturers to produce micro-milling cutting tools with small diameters and sharp edge radii. Generally, manufacturing cutting tools with micro-scale dimensions increases their cost. Therefore, attention must be paid to choosing suitable cutting conditions to avoid tool breakage, quick tool wear, chatter and poor surface finish. Usually, tool breakage occurs when the cutting forces are very high. High run-out and chatter can also enhance the damage processes of the cutting tool. Fast tool wear can be observed due to the presence of high cutting forces, high temperatures, chatter and adhesion. Poor surface finish is usually observed due to the presence of chatter, worn edge radii, high run-out and ploughing dominant cutting (when there is no chip formation and the material is mainly ploughed). Accurate prediction and proper consideration of the cutting forces can significantly reduce the negative effects caused in micro-milling.

Many researchers have worked on the development of analytical and mechanistic models for predicting micro-milling forces. Waldorf et al. [1] have developed a slip-line field to model the ploughing components of the cutting force. A series of experiments have been done on 6061-T6 aluminium using tools with different edge radii. Ko et al. [2] have developed an approximate size effect model using instantaneous cutting coefficients for an endmill with multiple flutes. The size effect is identified when the cutting coefficient tends to become non-linear for small values of

the uncut chip thickness. Vogler et al. [3] have developed a mechanistic model for micro-endmilling that explicitly accounts for the different phases while machining heterogeneous material. Kim et al. [4] have developed a static model of chip formation in micro-milling processes describing the intermittency of chip formation observed at low feed rates for brass. Kang et al. [5] have developed an analytical mechanistic model of micro-endmilling for predicting the cutting forces which considers the tool–workpiece contact at the flank face for aluminium. Bissacco et al. [6] have developed a theoretical model for cutting force prediction in micro-milling, taking into account the cutting edge radius size effect, the run-out and the deviation of the chip flow angle from the inclination angle steel for (UHB11, 0.46%C) and an aluminium alloy (6082T6). Malekian et al. [7] have investigated mechanistic modelling of micro-milling forces, with consideration of the effect of ploughing, elastic recovery, run-out and dynamics for Al6061-T6 material. A ploughing force model that takes the effect of elastic recovery into account has been developed based on the interface volume between the tool and the workpiece. Afazov et al. [8] have predict the cutting forces in micro-milling of AISI 4340 steel considering the run-out effect, cutting velocity, tool edge radius, material behaviour, etc. Very good agreement has been reported between predicted and experimentally measured forces for wide range of feed rates and spindle speeds.

In general, some steels are annealed to low material hardness when supplied. A typical example is AISI H13 steel which requires further heat treatments to achieve the required hardness for the corresponding application. AISI H13 steel has good abrasion resistance. It also resists softening at temperatures up to 550°C. It is widely used in industry with typical applications in hot work punches (44–48 HRC), blanking tools and bending dies (50–52 HRC), swaging dies (53–55 HRC), forging and extrusion dies (46–49 HRC), die casting (52–54 HRC), injection moulding and others on both macro- and micro-scale levels [9]. Research for predicting the cutting forces in conventional macro-scale machining has been carried out for AISI H13 steel at different hardnesses [10–12]. Surface finish investigations of AISI H13 have also been the subject of research [13, 14]. Generally, AISI H13 material behaves differently at different hardnesses which can influence the cutting forces in macro- and micro-scale machining and process behaviour respectively. Aramcharoen and Mativenga [15] have experimentally investigated how the uncut chip thickness and cutting edge radius affect the specific cutting force, surface finish and burr formation in micro-scale machining of AISI H13. Also, the effect of different micro-endmill geometries on product quality has been explored. Uriarte et al. [16] have presented some modifications to a mechanistic model for predicting micro-milling cutting forces and performed experimental validation by micro-milling AISI H13 hardened up to 60 HRC using two-flute carbide micro-endmills at feed rates of 0.25 and 0.75 μm per tooth.

Despite the conducted research, there are still knowledge gaps in modelling, investigation and experimental validation of micro-milling cutting forces of AISI H13 steel at wide range of cutting conditions and material hardnesses. The objective of this paper is to predict the micro-milling cutting forces of AISI H13 steel at material hardnesses between 35and 60 HRC and experimentally validate the predicted micro-milling cutting forces. The paper also focuses on material modelling of AISI H13 steel considering high strain rates at material hardnesses in the range 35–60 HRC. The main contribution of the paper is to accurately predict the micro-milling cutting forces for wide range of cutting conditions (feed rates, spindle speeds and depth of cuts) and material hardnesses of the AISI H13 steel which can be used for tool wear and chatter calculations or be directly used by practitioners for specific applications.

2 Overview of methodology

Figure 1 shows the methodology overview of this study. First, features of the micro-milling cutting tool (edge radius, rake angle, clearance angle) and the run-out parameters are measured. The edge radius, rake angle and clearance angle are used to model the cutting tool in FE model of orthogonal cutting. Workpiece material model is implemented in the FE model of orthogonal cutting to describe the AISI H13 behaviour at different strains, strain rates, temperatures and hardnesses. The run-out parameters are used as an input into the uncut chip thickness model which considers the full kinematics of the cutting tool. The results from the FE model of orthogonal cutting and the uncut chip thickness model are incorporated to predict the micro-milling cutting forces. An experimental programme is conducted to validate the predicted micro-milling cutting forces. Heat treatment procedure is employed to achieve certain hardness of the AISI H13 workpiece used in the experimental programme.

3 FE modelling of orthogonal cutting

Orthogonal cutting is simulated in a dynamic thermo-mechanical FEA using an explicit integration in ABAQUS/Explicit [17]. The explicit dynamic FEA is based on the implementation of an explicit integration rule together with the use of diagonal element mass matrices. The equations of motion for the body are integrated using the explicit central difference integration rule. The micro-milling process can be also simulated using FEA where the uncut chip thickness varies from tool teeth engaging point to the exit point and the transition state for the force prediction can be achieved. Such models are computationally very expensive and predict the cutting forces for specific cutting conditions. The

Fig. 1 Methodology diagram

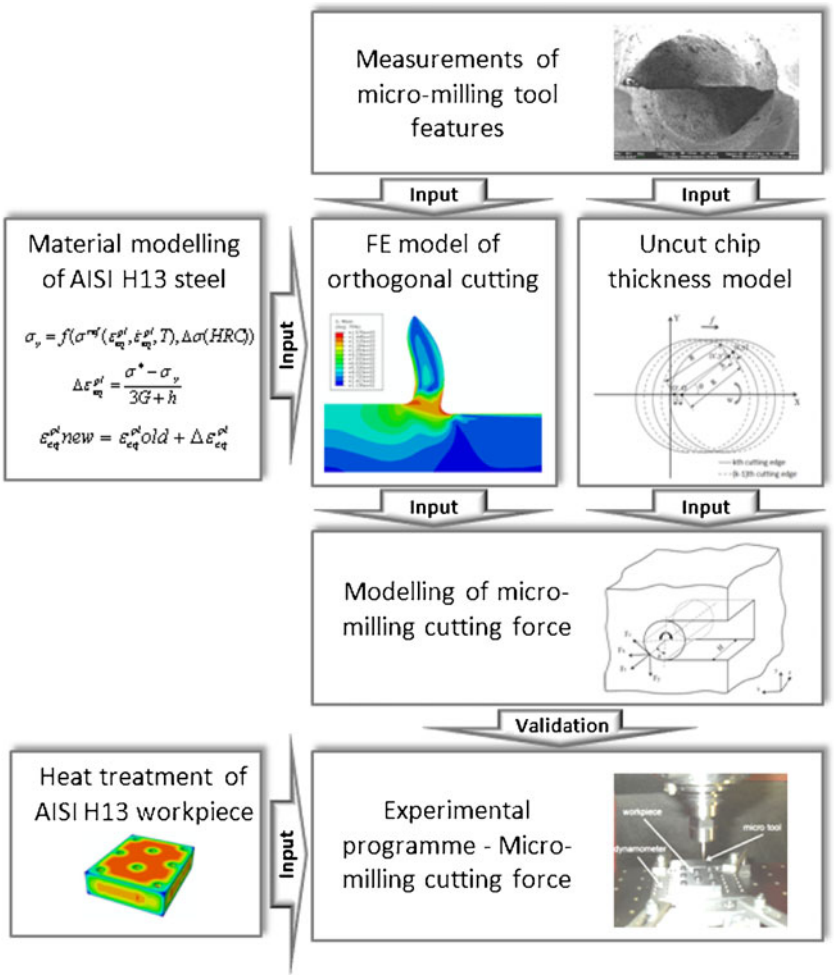

orthogonal cutting is used to obtain the cutting forces at constant uncut chip thickness. The transition state for the force prediction for different cutting conditions is achieved by describing the predicted cutting forces from the orthogonal cutting FEA with an analytical equation which can be used for further predictions of tool wear and chatter.

3.1 Geometry and mesh

Figure 2 shows a schematic of orthogonal cutting process with cutting tool profile captured with SEM/FIB CrossBeam workstation (NVision 40: Carl Zeiss SMT). In the FE model, the tool is modelled as an isothermal rigid body represented by a reference point (RP). The geometry of the tool is modelled based on SEM measurements of the cutting tool teeth. The edge shape of the tool is approximated as a radius (r) of 3.5 μm and the rake angle (α) is estimated to be 8°. Plane strain conditions are used within the FEA in this study. The workpiece is modelled as a rectangular block and meshed with four node bilinear temperature-displacement elements with reduced integration and hourglass control. The workpiece has 12,000 elements. Element thickness (a_p^{orth}) of 1 mm is applied to the model which is used as a reference when different depths of cut are investigated. Arbitrary Lagrangian–Eulerian adaptive meshing is used to prevent distortion of elements.

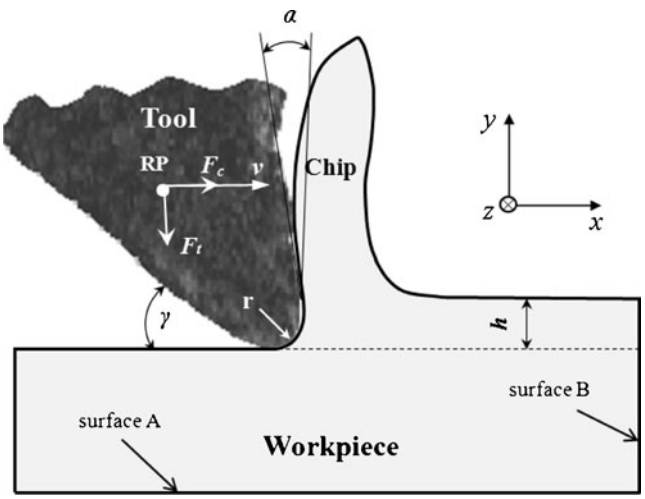

Fig. 2 Schematic of orthogonal cutting process

3.2 Boundary conditions and loads

The nodes of surface A are constrained in x and y directions while the nodes of surface B are constrained in x direction. The rotation in the x–y plane and the movement in the y direction of the tool are constrained at the RP. This allows tool movement only in the cutting direction. To decrease the effect of the boundary conditions, the dimensions of the workpiece are kept large enough to maintain a steady-state cutting condition. Different linear cutting velocities in the range 104.7–4,723 mm/s are applied at the RP in the cutting direction.

Room temperature is applied to the workpiece as an initial condition. Since the cutting velocity is very high and the process is performed for a short period of time, the orthogonal cutting can be assumed as adiabatic. Therefore, only conduction is considered in the FE model whilst convection and radiation are neglected. Similar to other researchers, an inelastic heat fraction of 90% is used in the model [18]. This means that 90% of the plastic work will be converted into heat. Also, the heat generation due to the contact between the workpiece and the tool is implemented. The fraction of dissipated energy converted into heat is assumed to be 100% and the heat is distributed equally between the two surfaces in contact. The heat exchange between the workpiece and the tool is achieved by applying a heat transfer coefficient of 10,000 W/m^2°C based on the work carried out by Marbrouki et al. [19]. Coulomb friction law is used in the current study where a friction coefficient of 0.4 is applied between the workpiece and the coated tool represented as a rigid body based on the experimental work performed by Ozlu et al. [20].

3.3 Material model and properties

The material model used in the FE model of orthogonal cutting is an isotropic thermal–elastic–plastic model using the constitutive equation reported by Yan et al. [21]. The constitutive equation considers the influence of the workpiece hardness on the flow stresses as follows:

$$\sigma_y = f\left(\sigma^{\text{ref}}\left(\varepsilon_{\text{eq}}^{\text{pl}}, \dot{\varepsilon}_{\text{eq}}^{\text{pl}}, T\right), \Delta\sigma(\text{HRC})\right) \quad (1)$$

Table 1 Johnson–Cook material constants for AISI H13 material [21]

A (MPa)	B (MPa)	E	n	m
908.54	321.39	0.028	0.278	1.18

Table 2 Constants for the additional component of stress Δσ(HRC) [21]

Hardness (HRC)	C	D
35	−9.87	−544.76
40	−7.89	−395.76
46	0	0
50	5.92	221.8
55	19.74	489.49
60	32.89	774.26

where the reference flow stresses $\sigma^{\text{ref}}\left(\varepsilon_{\text{eq}}^{\text{pl}}, \dot{\varepsilon}_{\text{eq}}^{\text{pl}}, T\right)$ and the additional component of stress Δσ(HRC) can be given by:

$$\sigma^{\text{ref}} = \left(A + B\left(\varepsilon_{\text{eq}}^{\text{pl}}\right)^n\right)\left(1 + E\ln\dot{\varepsilon}_{\text{eq}}^{\text{pl}^*}\right)\left(1 - (T^*)^m\right) \quad (2)$$

$$\Delta\sigma = C\ln\left(\varepsilon_0 + \varepsilon_{\text{eq}}^{\text{pl}}\right) + D \quad (3)$$

The reference flow stresses is described by the Johnson–Cook (JC) constitutive equation which is strain rate and

Table 3 Mechanical and physical material properties for AISI H13 [27]

Modulus of elasticity, E (GPa)	T	E
	20	207
	93	200
	300	186
	540	158
Poisson's ratio, υ (–)	0.3	
Density, ρ (kg/m^3)	7,800	
Specific heat capacity, c_p (J/kg°C)	T	c_p
	20	430
	100	470
	200	521
	300	571
	400	621
	500	673
	600	722
Thermal conductivity, k (W/m°C)	T	k
	27	17.6
	204	23.4
	427	25.2
	649	26.8
Melting temperature, T_{melt} (°C)	1,490	
Linear coefficient of thermal expansion, ζ (μm/m°C)	T	ζ
	93	10.4
	204	11.3
	316	12.4
	427	13.1
	538	13.5

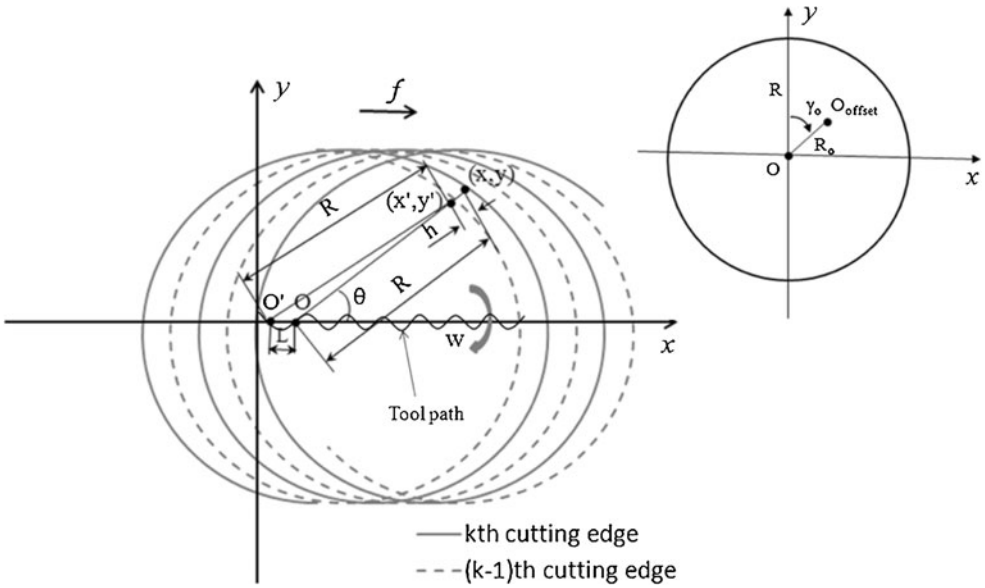

Fig. 3 Trajectory of the k^{th} and the $(k\text{-}1)^{th}$ tool edges in the x–y Cartesian coordinate system and cutting tool centre offset

temperature-dependent viscoplastic material model. The final stress flow constitutive equation can be given by:

$$\sigma_y = \left(A + B\left(\varepsilon_{eq}^{pl}\right)^n + C\ln\left(\varepsilon_0 + \varepsilon_{eq}^{pl}\right) + D\right) \times \left(1 + E\ln\dot{\varepsilon}_{eq}^{pl^*}\right)\left(1 - (T^*)^m\right) \quad (4)$$

where $\varepsilon = 10^{-3}$ is the reference strain, $\dot{\varepsilon}_{eq}^{pl^*} = \dot{\varepsilon}/\dot{\varepsilon}_0$ is the dimensionless strain rate for $\dot{\varepsilon}_0 = 1.0s^{-1}$, A is the initial yield stress, B is the hardening modulus, n is the hardening exponent, E is the strain rate dependency coefficient and m is the thermal softening coefficient (see Table 1). The homologous temperature can be given by $T^* = (T - T_r)/(T_{melt} - T_r)$, where T is the reference temperature, T_r is the transition or room temperature, T_{melt} is the melting temperature. The constants C and D are the function of the initial workpiece hardness. The constant values at different material hardnesses are given in Table 2. Temperature-dependent mechanical and physical properties are used in the FE model, as shown in Table 3.

An important feature of the micro-milling process is the presence of size effect or dependence of strength on the scale of deformation as observed by a number of researchers. This is mainly due to the material behaviour at micro-scale since the feed rates in micro-milling are comparable with the material grain sizes. Generally, the size effect can

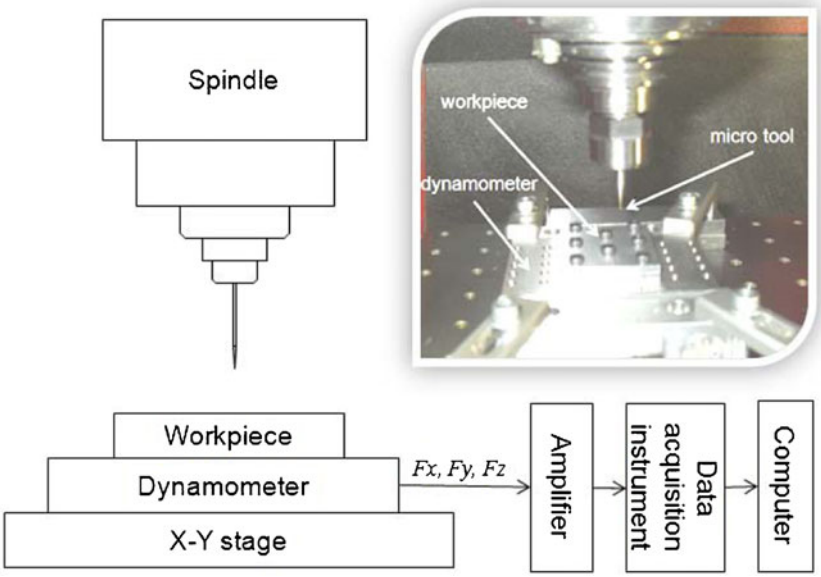

Fig. 4 Experimental setup

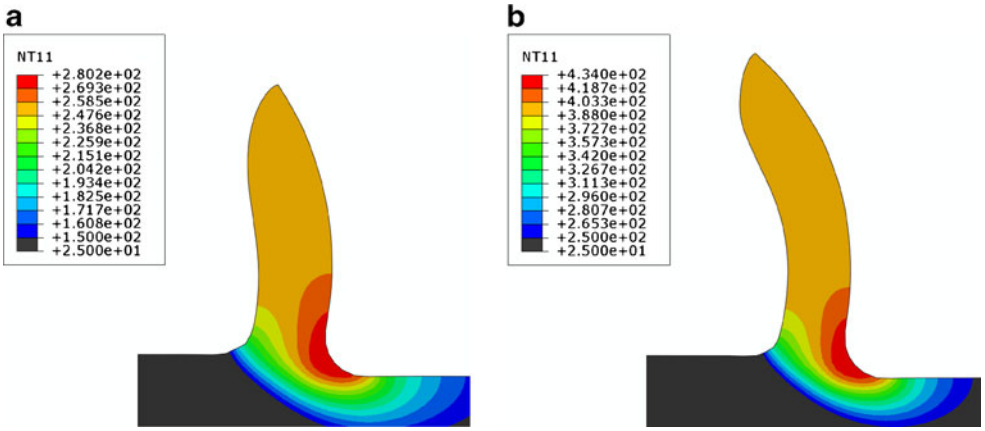

Fig. 5 Chip formation and temperature distribution for uncut chip thickness of 2 μm and velocity of 1,571 mm/s at: **a** hardness of 40 HRC; **b** hardness of 60 HRC

be described as non-linear increase of the specific cutting energy at different micro-machining cutting conditions. Karpat [22] reported four explanations that relate the size effect to the material strengthening mechanisms due to: (1) the decreasing number of defects in microstructure, (2) the increasing strain rate at the primary shear zone, (3) the effect of thermal softening and (4) the effect of strain gradient plasticity at the deformation zones at low uncut chip thickness. Also, the size effect is caused by the negative rake angle generated by the edge radius. In a previous study for prediction of micro-milling cutting forces of AISI 4340 steel, the authors modelled the material behaviour in micro-cutting using the JC constitutive equations where very good correlation between predicted and experimental results have been achieved [8]. Also, Afazov et al. [23] considered the size effect in determining the micro-milling cutting forces of Ti6Al4V alloy by modelling the material stress flow using the JC constitutive equation and the strain gradient plasticity theory. It has been observed that the material model using the strain gradient plasticity results with better correlation with the experimentally obtained micro-milling cutting forces for feed rates less or equal to 6 μm/tooth, while the JC material model predicts more accurately the micro-milling cutting forces for feed rates of 12 μm/tooth. Inspired by the results for AISI 4340 steel using the JC material model in [8], the material model from Eq. 4 is considered suitable to account for the size effects in this study.

3.4 Implementation of constitutive material model

The constitutive Eq. 4 is implemented into ABAQUS/Explicit by the user-defined subroutine VUMAT written in FORTRAN code. To implement Eq. 4 into the VUMAT subroutine, the elasto-plastic material behaviour needs to be defined for each integration/material point of the FE model. For elastic behaviour in time incremental FEA, the constitutive law can be given in vector/matrix form by:

$$\{\sigma^{\text{new}}\} = \{\sigma^{\text{old}}\} + [D]\{\Delta\varepsilon\} \tag{5}$$

where $\{\sigma^{\text{new}}\}$ and $\{\sigma^{\text{old}}\}$ are column vectors containing the new and the old tensor stresses, $\{\Delta\varepsilon\}$ is a column vector containing the incremental tensor strains and $[D]$ is a stress–strain stiffness matrix. For an isotropic material, the stress–strain stiffness matrix consists of

Table 4 Constants for the cutting forces from Eq. 13 for different material hardnesses

Constants	35 HRC		40 HRC		46 HRC		50 HRC		55 HRC		60 HRC	
	F_c	F_t	F_c	F_t	F_c	F_t	F_c	F_t	F_c	F_t	F_c	F_t
$p_1\times(10^3)$	12	15	23.35	19.4	19.28	20.7	25.9	23.3	33.94	27	37.24	29.3
$p_2\times(10^{-2})$	0	0	−6.6	0	−2.7	0	−4.49	0	−6.97	0	−6.48	0
$p_3\times(10^{-4})$	−1.6	−0.3	−1.6	−0.3	−1.6	−0.3	−1.6	−0.3	−1.6	−0.3	−1.6	−0.3
$p_4\times(10^{-4})$	0	0	−1	0	−2	0	−3	0	−2	0	−5	0
p_5	4.7	4.6	5.87	6.3	6.43	7.2	7.89	8	8.93	9.5	10.25	11
p_6	−4	−9	−4.5	−10.5	−10	−12.5	−5	−9	−5	−7	−4.5	−6.5

relationships between modulus of elasticity (E) and Poisson's ratio (v). The temperature-dependent modulus of elasticity is introduced within the VUMAT subroutine by using a linear interpolation technique for the

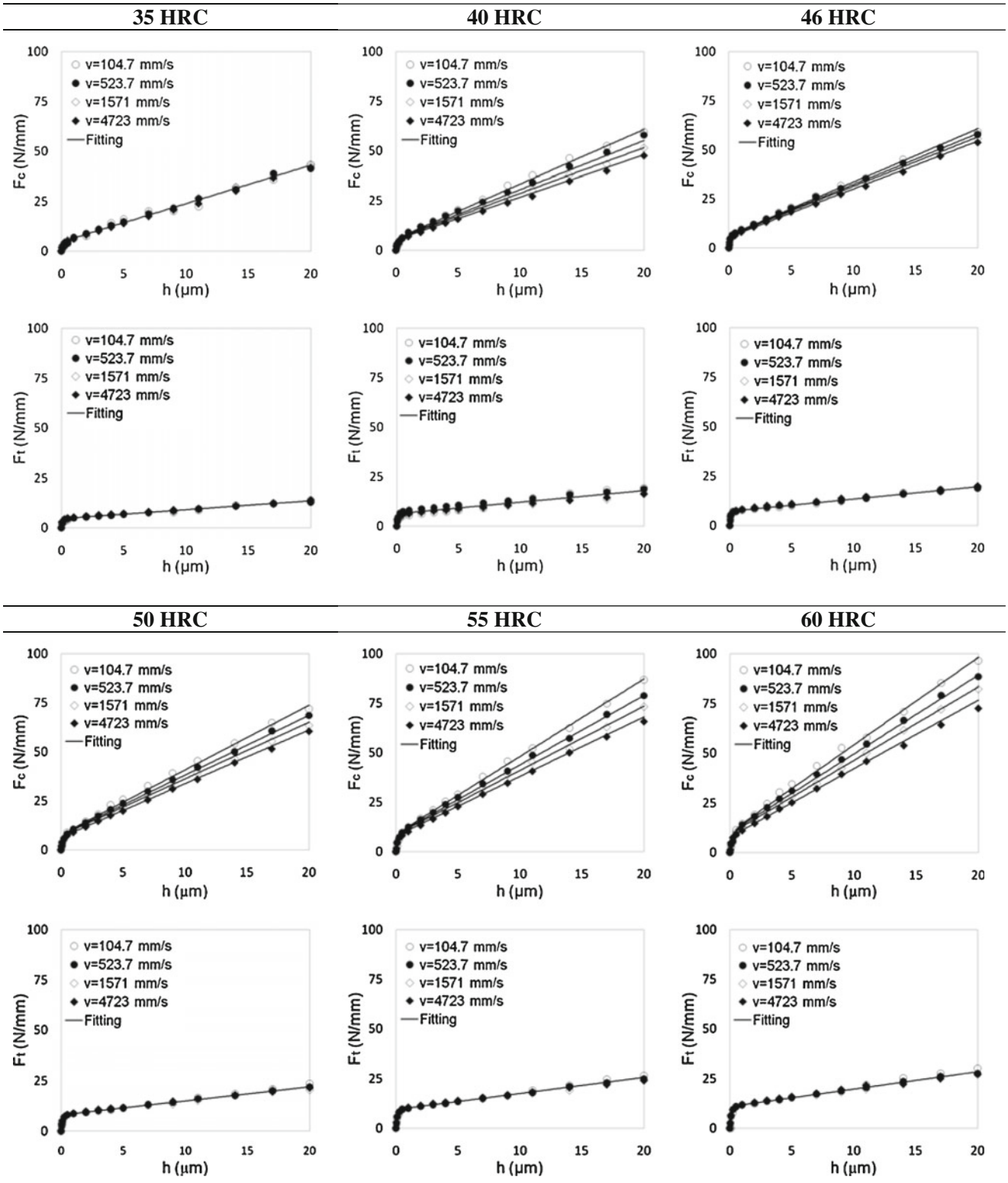

Fig. 6 FE-predicted cutting forces in cutting and tangential directions for hardnesses between 35 and 60 HRC

corresponding temperature of the material/integration point. It is possible to decompose the stress vector $\{\sigma^{new}\}$ into a deviatoric stress vector $\{S\}$ and a hydrostatic vector $\{\sigma_m\}$ so that

$$\begin{bmatrix} S_{11} & S_{12} & S_{13} \\ S_{21} & S_{22} & S_{23} \\ S_{31} & S_{32} & S_{33} \end{bmatrix} = \begin{bmatrix} \sigma_{11}^{new} & \sigma_{12}^{new} & \sigma_{13}^{new} \\ \sigma_{21}^{new} & \sigma_{22}^{new} & \sigma_{23}^{new} \\ \sigma_{31}^{new} & \sigma_{32}^{new} & \sigma_{33}^{new} \end{bmatrix} - \begin{bmatrix} \sigma_m & 0 & 0 \\ 0 & \sigma_m & 0 \\ 0 & 0 & \sigma_m \end{bmatrix} \tag{6}$$

where the hydrostatic stress is given by:

$$\sigma_m = \frac{1}{3}\left(\sigma_{11}^{new} + \sigma_{22}^{new} + \sigma_{33}^{new}\right) \tag{7}$$

The equivalent Von Mises stresses can be then given by:

$$\sigma^* = \sqrt{\frac{2}{3}\left({S_{11}}^2 + {S_{22}}^2 + {S_{33}}^2 + 2\left({S_{12}}^2 + {S_{13}}^2 + {S_{23}}^2\right)\right)} \tag{8}$$

Plasticity occurs when

$$\sigma^* - \sigma_y > 0 \tag{9}$$

The increment of equivalent plastic strain is obtained explicitly through [24]

$$\Delta\varepsilon_{eq}^{pl} = \frac{\sigma^* - \sigma_y}{3G + H} \tag{10}$$

where $H = d\sigma_y/d\varepsilon_{eq}^{pl}$ is the plastic hardening at the beginning of the increment and $G=E/2(1+\nu)$ is the shear modulus. The equivalent plastic strain at time $t+\Delta t$, after defining the incremental plastic strain from Eq. 10, is updated by:

$$\varepsilon_{eq}^{pl}\text{new} = \varepsilon_{eq}^{pl}\text{old} + \Delta\varepsilon_{eq}^{pl} \tag{11}$$

The yield stress (σ_y^{new}) at time $t+\Delta t$ is then updated using Eq. 4. The stresses for the plain strain model are updated by:

$$\begin{aligned} \sigma_{11} &= \frac{S_{11}\sigma_y^{new}}{\sigma_y^{new} + 3G\Delta\varepsilon_{eq}^{pl}} + \sigma_m \\ \sigma_{22} &= \frac{S_{22}\sigma_y^{new}}{\sigma_y^{new} + 3G\Delta\varepsilon_{eq}^{pl}} + \sigma_m \\ \sigma_{33} &= \frac{S_{33}\sigma_y^{new}}{\sigma_y^{new} + 3G\Delta\varepsilon_{eq}^{pl}} + \sigma_m \\ \sigma_{12} &= \frac{\sigma_{12}\sigma_y^{new}}{\sigma_y^{new} + 3G\Delta\varepsilon_{eq}^{pl}} \end{aligned} \tag{12}$$

Finally, the specific internal energy and the dissipated inelastic specific energy for the plain strain FE model are updated.

4 Modelling of micro-milling cutting forces

The authors described the relationship between cutting forces, uncut chip thickness and cutting velocity obtained from FE model of orthogonal cutting of AISI 4340 steel by [8]:

$$F_{c,t} = (p_1 v^{p_2})[1 - \exp(p_3 h)] + (p_4 v + p_5)[1 - \exp(p_6 h)] \tag{13}$$

where the constants p_1, p_2, p_3, p_4, p_5 and p_6 are obtained after curve fitting procedure.

The cutting velocity from the orthogonal cutting model is represented as a tangential velocity of the cutting tool and can be given by:

$$v = w\left(R - 0.5h \times 10^{-3}\right) \tag{14}$$

The unit of the uncut chip thickness (h) in Eqs. 13 and 14 is micrometer (μm). Considering the full kinematics of

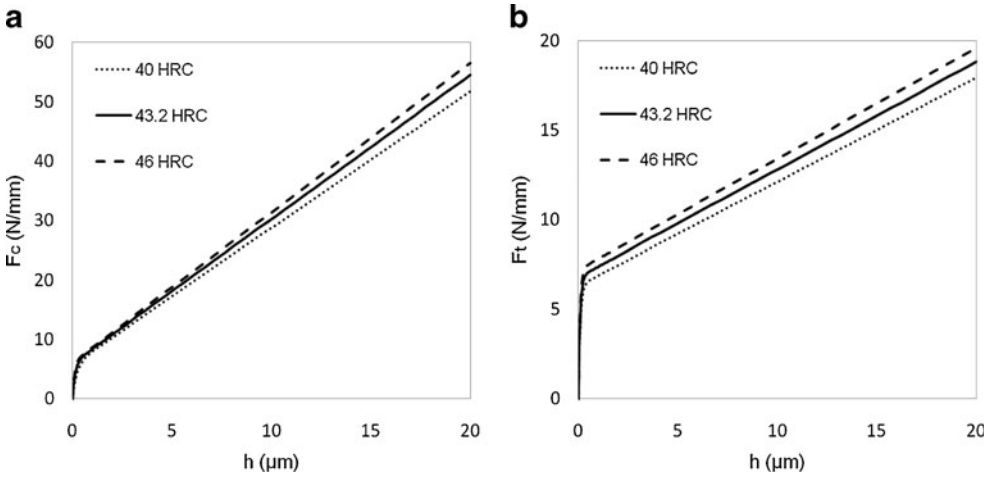

Fig. 7 Comparison between the FE-predicted forces at 40 and 46 HRC and the approximated forces at 43.2 HRC at velocity of 1,500 mm/s in the: **a** cutting direction; **b** tangential direction

the cutting tool including the run-out effect (see Fig. 3), the uncut chip thickness h (in millimetre) can be given by [8]:

$$h = R + L\sin(wt - 2\pi k/K + \alpha_o) - \sqrt{R^2 - L^2\cos^2(wt - 2\pi k/K + \alpha_o)} \quad (15)$$

where R is the radius of the tool (in millimetre), w is the spindle angular velocity (radian per second), k is the flute number and K is the number of flutes. The distance L (in millimetre) and the angle α_o (radian) can be given by:

$$L = \sqrt{(x_o - x_{o'})^2 + (y_o - y_{o'})^2} \quad (16)$$

$$\alpha_o = \arctan\left(\frac{y_o - y_{o'}}{x_o - x_{o'}}\right) \quad (17)$$

The coordinates of nodes O and O′ can be given by:

$$x_{(O)} = \mathrm{ft} + R_o\sin(\mathrm{wt} + \gamma_o)$$
$$y_{(O)} = R_o\cos(\mathrm{wt} + \gamma_o) \quad (18)$$

$$x_{(O')} = \mathrm{ft}' + R_o\sin(\mathrm{wt}' + \gamma_o)$$
$$y_{(O')} = R_o\cos(\mathrm{wt}' + \gamma_o) \quad (19)$$

where f is the feed rate (millimetre per second), Ro is the run-out length (in millimetre), γ_0 is the run-out angle (radian) and t' is the time of the previous cutting edge. The time t' can be defined by solving Eq. 20 numerically using the Newton–Raphson method.

$$\begin{aligned} &R\tan(\mathrm{wt} - 2\pi k/K)\cos(\mathrm{wt}' - 2\pi(k-1)/K) \\ &+R_o\tan(\mathrm{wt} - 2\pi k/K)\cos(\mathrm{wt}' + \gamma_o) \\ &-R_o\tan(\mathrm{wt} - 2\pi k/K)\cos(\mathrm{wt} + \gamma_o) \\ &-\mathrm{ft}' + \mathrm{ft} - R\sin(\mathrm{wt}' - 2\pi(k-1)/K) \\ &-R_o\sin(\mathrm{wt}' + \gamma_o) + R_o\sin(\mathrm{wt}+\gamma_o) = 0 \end{aligned} \quad (20)$$

The micro-milling cutting forces in the cutting and tangential directions for given angle of rotation or time are obtained by substituting Eqs. 14 and 15 into Eq. 13. The forces in the x and y directions can be given by:

$$\begin{bmatrix} F_x \\ F_y \end{bmatrix} = \frac{a_p}{a_p^{\mathrm{orth}}}\begin{bmatrix} \sin\theta & \cos\theta \\ -\cos\theta & \sin\theta \end{bmatrix}\begin{bmatrix} F_t \\ F_c \end{bmatrix} \quad (21)$$

where a_p is the depth of cut (0.1 mm in the current study), a_p^{orth} is the element thickness from the orthogonal FE model (1 mm at the current study) and θ is the angle of rotation. In Eq. 21, the effect of the helix angle is not considered based on the assumption that the helix angle does not significantly affect the cutting forces in the cutting and tangential directions for small depth of cut.

5 Experimental programme

The supplied AISI H13 steel with hardness of 8 HRC is first heat-treated in order to achieve an adequate material hardness. The following processes are carried out: (1) The material is pre-heated to 750°C and then raised quickly to 1,035°C; (2) The material is cooled in air down to room temperature; (3) heated to 610°C and kept in the furnace for 30 min and air-cooled down to room temperature afterwards; (4) heated again to 610°C and kept for 30 min in the furnace and finally cooled down to room temperature in air. The achieved material hardness measured on a hardness test machine on Rockwell C scale is 43.2 HRC after grinding the layers of oxidised material.

An ultra precision five-axis milling machine KERN Evo with computer numerical control (CNC) is utilised to perform the experimental programme. Figure 4 shows the experimental setup. A Kistler dynamometer (9256C2) is mounted on the five-axis KERN machine to measure the micro-milling cutting forces. The sensitivity of the dynamometer is 26 pC/N in the x and y directions.

Based on FE frequency analyses, the workpiece is designed with dimensions of 36 mm width, 40 mm height, 7 mm thickness and eight holes each of 3-mm diameter and clamped with eight bolts. A two-flute TiN-coated tungsten tool with diameter of 500 μm and flute length of 1 mm is used. The static run-out is measured at the tool tip before performing each of the cutting trials using a dial indicator attached to the CNC machine. A run-out length (R_o) in the range 0.1–0.5 μm and a run-out angle (γ_o) of 45° are determined. The zero point in the z direction is found by moving the cutting tool down to the workpiece very slowly until a jump of the acoustic emission signal is detected. Numerous dry cutting trials are performed at spindle angular velocities of 25,000 and 50,000 rpm, feed rates between 0.5 and 10 mm/s and depth of cut of 100 μm on the heat-treated workpiece with hardness of 43.2 HRC.

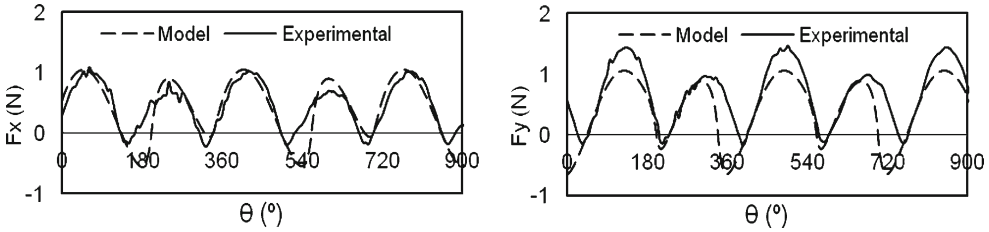

Fig. 8 Forces at w= 25,000 rpm and f=0.5 mm/s; h_{max}=0.81 μm

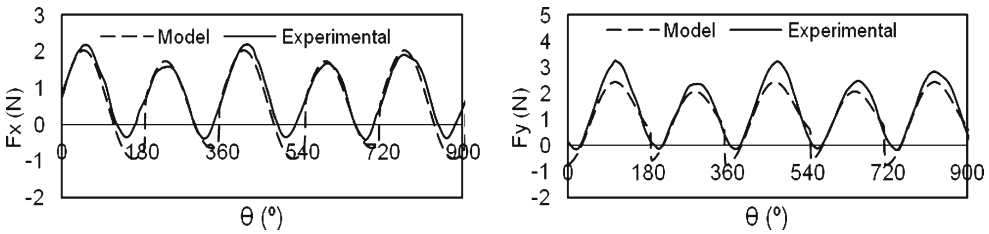

Fig. 9 Forces at w= 25,000 rpm and f=5 mm/s; h_{max}=6.7 μm

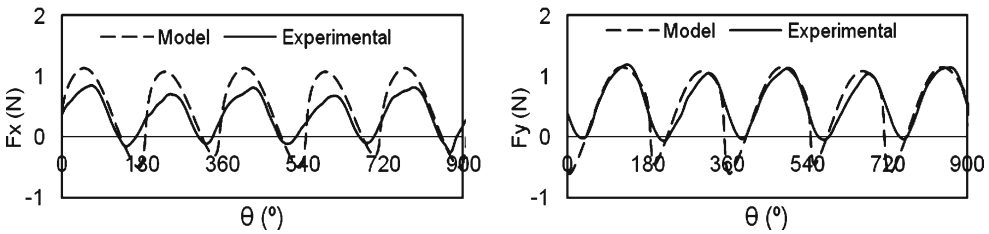

Fig. 10 Forces at w= 50,000 rpm and f=2 mm/s; h_{max}=1.34 μm

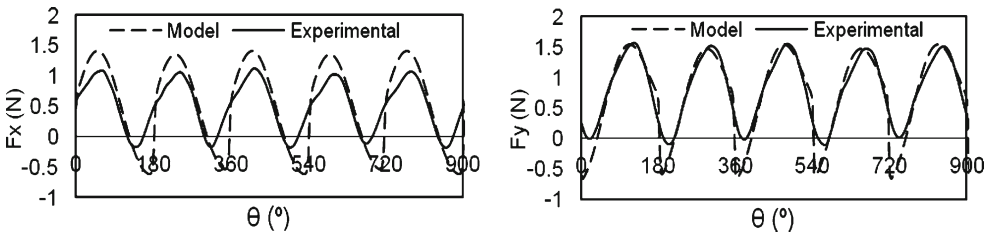

Fig. 11 Forces at w= 50,000 rpm and f=5 mm/s; h_{max}=3.14 μm

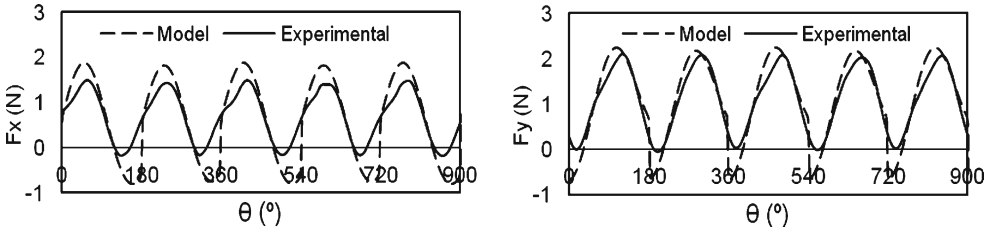

Fig. 12 Forces at w= 50,000 rpm and f=10 mm/s; h_{max}=6.14 μm

6 Results and discussion

The results presented in this section are mainly focused on the predicted and experimentally measured cutting forces, but also, results related to temperature introduced during cutting and chatter are discussed. Figure 5 shows the chip formation and the temperature distribution for uncut chip thickness of 2 μm and cutting velocity of 1,571 mm/s at material hardnesses of 40 and 60 HRC. It can be seen for both hardnesses that the maximum temperature is located at the contacting area between the cutting tool edge and the workpiece. The maximum temperature at hardness of 60 HRC is 434°C, while at of 40 HRC, the temperature is 280°C. This shows that the temperature during cutting increases by increasing the material hardness. It is also observed that the temperature increases by increasing the uncut chip thickness. For example, temperature of 602°C is predicted for uncut chip thickness of 14 μm and cutting velocity of 1,571 mm/s at material hardnesses of 60 HRC. The predicted temperatures during cutting can be considered in defining the cutting conditions in order to avoid fast wear of the cutting tool at higher temperatures.

Three hundred sixty FEAs are run to describe the relationship between cutting forces (in tangential and cutting directions), uncut chip thickness, cutting velocity and material hardness. In terms of computational time for cutting length of 68 μm of the tool, the FE models with cutting velocity of 4,723 mm/s run for about 25–30 min depending on the magnitude of the uncut chip thickness, while the FE models with cutting velocity of 104.7 mm/s run for about 1 day. The FEA have been submitted to high-performance computer with multi-CPUs where each analysis is computed on single CPU. The relationship between FE-predicted cutting forces, uncut chip thickness and cutting velocity for each material hardness is defined with Eq. 13 which describes the ploughing and shear dominant forces. The ploughing dominant phenomenon is observed until the point when the ratio between the uncut chip thickness and the edge radius of the cutting tool, known as cutting edge ratio, has reached certain value. The cutting edge ratio can vary in the range 0.09–0.4 for different materials, cutting conditions and tool–workpiece interactions as reviewed in [15]. It is characterised by pushing the material without forming a chip which causes both plastic deformation and elastic recovery or springback effect [1]. Ploughing also results with poor surface finish and burr formation [25]. The shear dominant phenomenon is characterised by forming chips during cutting. Both ploughing and shear dominant phenomena exist in micro-milling since the uncut chip thickness varies at different angles of rotation. The six constants in Eq. 13 are defined by a fitting technique described in [8]. The constants are obtained for material hardnesses of 35, 40, 46, 50, 55 and 60 HRC and given in Table 4. The FE-predicted cutting forces and the fitted curves are shown in Fig. 6. The unit (Newton millimetre) represent the cutting forces obtained for 1-mm element thickness of the plain strain FE model of orthogonal cutting. Also, the cutting forces are predicted for uncut chip thicknesses for up to 20 μm. It should be mentioned that feed rates of 20 μm/tooth can cause brakeage of the cutting tools. On the other hand, the predicted forces at higher uncut chip thicknesses can be used for tools with larger diameters (e.g. 1–2 mm).

It can be seen that by increasing the velocity, the forces in the cutting direction decrease. This is caused mainly by the higher induced temperatures which soften the material and the inertia effect at higher velocities (Fig. 6). The forces in the tangential direction and the cutting direction at 35 HRC are velocity-independent. It can be also seen that the forces in both cutting and tangential directions increase by increasing the material hardness. The material hardness can be incorporated in Eq. 13 by describing the relationship between each constant from Table 4 as function of the material hardness. In this study, the constants $p_1,p_2,\ldots,p_6$ from Eq. 13 at hardness of 43.2 HRC are defined using a linear interpolation. As an example, Fig. 7 shows the predicted cutting forces for material hardnesses of 40 and 46 HRC and the approximated cutting forces at 43.2 HRC using a linear interpolation between the constants from Eq. 13 obtained

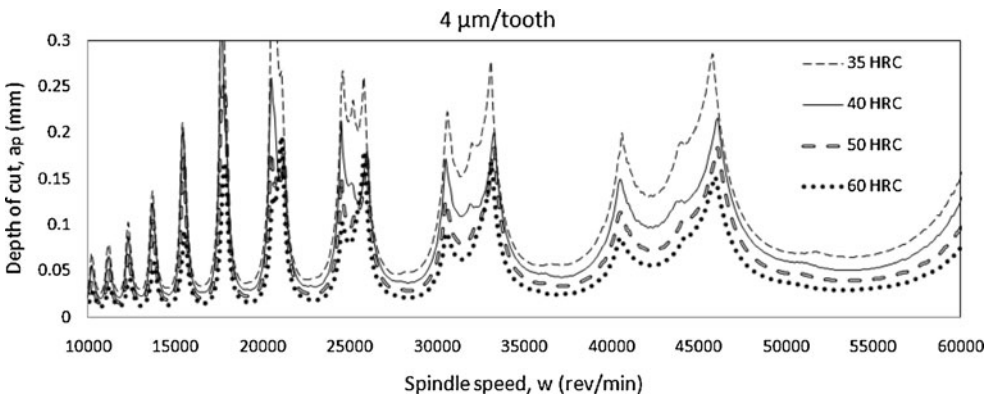

Fig. 13 Stability lobes for AISI H13 at feed rate of 4 μm/flute and different material hardnesses

at 40 and 46 HRC. It can be seen that the approximated curve describing the forces in the cutting and tangential direction as function of the uncut chip thickness for 43.2 HRC is located between the curves representing the hardnesses of 40 and 46 HRC.

The approximated constants from Eq. 13 for 43.2 HRC are used for prediction of the micro-milling cutting forces in order to compare the results with the measured micro-milling cutting forces of the heat-treated workpiece with hardness of 43.2 HRC. Figures 8, 9, 10, 11 and 12 show comparison between the predicted and experimentally measured micro-milling cutting forces for five cutting conditions. It can be seen that the predicted and measured cutting forces arrived at good agreement. The effect of the run-out phenomenon on the cutting forces can also be seen, especially in Figs. 8 and 9.

Furthermore, the micro-milling cutting force model and results in this study are used to investigate the process stability at different material hardnesses. Stable micro-milling is observed with no presence of self-excited vibration between the cutting tool and the workpiece, known as chatter. Chatter is characterised by poor surface quality and fast tool wear. The chatter model in time domain solution developed by the authors is used to predict the stability lobes at different hardnesses of the AISI H13 steel [26]. The micro-milling force model with the validated force constants for AISI H13 material using Eq. 13 and the dynamics of the tool-holder-spindle assembly at the tool tip [26] for the tool used in this study are incorporated into the chatter model. Figure 13 shows the predicted chatter stability lobes at feed rate of 4 μm/flute and material hardnesses of 35, 40, 50 and 60 HRC. It can be seen that the stability limits decrease by increasing the material hardness. This can be explained with the increase of the cutting forces at high material hardnesses. The predicted stability limits can be directly used for selection of stable cutting conditions.

7 Conclusions

Material model considering the stress flow as a function of the stain, strain rate, temperature and the hardness of AISI H13 steel has been modelled and implemented into ABAQUS/Explicit FE code using the VUMAT user-defined subroutine using the elasto-plastic constitutive equations and algorithms.

FE model of orthogonal cutting has been successfully developed to predict the relationship between cutting forces, uncut chip thickness and cutting velocity at material hardnesses of 35, 40, 46, 50, 55 and 60 HRC. The micro-milling cutting forces have been determined based on the FE-predicted forces and the calculated uncut chip thickness considering the full kinematics of the micro-milling tool including the run-out effect. It has been observed that the cutting forces increase by increasing the material hardnesses.

The predicted micro-milling cutting forces have been validated with experimentally measured results at different spindle speeds and feed rates. The results showed very good agreement between predicted and experimentally measured micro-milling cutting forces.

Chip formation and workpiece temperature distribution have been predicted using the FE model of orthogonal cutting. It has been observed that the maximum temperature is located at the contact area of the cutting tool edge and the workpiece material. It has been also observed that by increasing the material hardness, the micro-milling-induced temperature increases while the stability limits decrease.

Acknowledgements The authors wish to acknowledge the Nottingham Innovative Manufacturing Research Centre (NIMRC) and the Engineering and Physical Sciences Research Council (EPSRC) for their financial support of the work.

References

1. Waldorf D, DeVor R, Kapoor S (1998) A slip-line field for ploughing during orthogonal cutting. J Manuf Sci Eng 120:693–699
2. Ko J, Yun W, Cho D, Ehmann K (2002) Development of a virtual machining system, part 1: approximation of the size effect for cutting force prediction. Int J Mach Tools Manuf 42:1595–1605
3. Vogler M, DeVor R, Kapoor S (2003) Microstructure-level force prediction model for micro-milling of multi-phase materials. J Manuf Sci Eng 125:202–209
4. Kim C, Mayor J, Ni J (2004) A static model of chip formation in microscale milling. J Manuf Sci Eng 126:710–718
5. Kang I, Kim JS, Kim JH, Kang M, Seo Y (2007) A mechanistic model of cutting force in the micro end milling process. J Mater Proc Technol 187–188:250–255
6. Bissacco G, Hansen H, Slunsky J (2008) Modelling the cutting edge radius size effect for force prediction in micro milling. CIRP Ann Manuf Technol 57:113–116
7. Malekian M, Park S, Jun M (2009) Modelling of dynamic micro-milling cutting forces. Int J Mach Tools Manuf 49:586–598
8. Afazov SM, Ratchev SM, Segal J (2010) Modelling and simulation of micro-milling cutting forces. J Mater Proc Technol 210:2154–2162
9. Corus Group, "Hot work tool steel—AISI H13", London, Corus Group
10. Qian L, Hossan MR (2007) Effect on cutting force in turning hardened tool steels with cubic boron nitride inserts. J Mater Proc Technol 191:274–278
11. Sartkulvanich P, Koppka F, Altan T (2004) Determination of flow stress for metal cutting simulation—a progress report. J Mater Proc Technol 146:61–71
12. Ng E-G, Aspinwall DK (2002) The effect of workpiece hardness and cutting speed on the machinability of AISI H13 hot work die steel when using PCBN tooling. J Manuf Sci Eng 124:588–594
13. Zhang S, Guo YB (2009) Taguchi method based process space for optimal surface topography by finish hard milling. J Manuf Sci Eng 131:051003
14. Nicola GL, Missell FP, Zeilmann RP (2010) Surface quality in milling of hardened H13 steel. Int J Adv Manuf Technol 49:53–62
15. Aramcharoen A, Mativenga PT (2009) Size effect and tool geometry in micromilling of tool steel. Precis Eng 33:402–440

16. Uriarte L, Azcárate S, Herrero A, Lopez LN, Lamikiz A (2008) Mechanistic modelling of the micro end milling operation. Proc IME Part B J Eng Manufact 222:23–33
17. ABAQUS/Explicit (2008) "Theory and analysis user's manual", Version 6.8-3
18. Longère P, Dragon A (2008) Evaluation of the inelastic heat fraction in the context of microstructure-supported dynamic plasticity modelling. Int J Impact Eng 35:992–999
19. Mabrouki T, Rigal J (2006) A contribution to a qualitative understanding of thermo-mechanical effects during chip formation in hard turning. J Mater Proc Technol 176:214–221
20. Ozlu E, Budak E, Molinari A (2009) Analytical and experimental investigation of rake contact and friction behavior in metal cutting. Int J Mach Tools Manuf 49:865–875
21. Yan H, Hua J, Shivpuri R (2007) Flow stress of AISI H13 die steel in hard machining. Mater Des 28:272–277
22. Karpat Y (2009) Investigation of the effect of cutting tool edge radius on material separation due to ductile fracture in machining. Int J Mech Sci 51:541–546
23. Afazov SM, Ratchev SM, Segal J (2011) Determination of cutting forces and process stability in micro-milling of Ti6Al4V alloy by considering the size-effect phenomenon. Micro Nano-Syst 3:199–209
24. Afazov S, Ratchev S, Segal J (2010) FE modelling of size-effect in micro-machining using the strain gradient plasticity theory. In: 7th International Conference on Multi-Material Micro Manufacture, Bourg en Bresse and Oyonnax, France, pp. 178–183
25. Mian AJ, Driver N, Mativenga PT (2009) Micromachining of coarse-grained multi-phase material. Proc IME B J Eng Manufact 223:337–385
26. Afazov S, Ratchev S, Segal J (2011) Effects of the cutting tool edge radius on the stability lobes in micro-milling. In: 13th CIRP Conference on Modelling of Machining Operations, Sintra, Portugal. pp. 859–868
27. Nasr M, Ng E, Elbestawi M (2008) A modified time-efficient FE approach for predicting machining-induced residual stresses. Finite Elem Anal Des 44:149–161